Author/s:
Balendhran, S;Hussain, Z;Shrestha, VR;Cadusch, J;Ye, M;Sefidmooye Azar, N;Kim, H;Ramanathan, R;Bullock, J;Javey, A;Bansal, V;Crozier, KB

Title:
Copper Tetracyanoquinodimethane (CuTCNQ): A Metal-Organic Semiconductor for Room-Temperature Visible to Long-Wave Infrared Photodetection

Date:
2021-08-18

Citation:
Balendhran, S., Hussain, Z., Shrestha, V. R., Cadusch, J., Ye, M., Sefidmooye Azar, N., Kim, H., Ramanathan, R., Bullock, J., Javey, A., Bansal, V. & Crozier, K. B. (2021). Copper Tetracyanoquinodimethane (CuTCNQ): A Metal-Organic Semiconductor for Room-Temperature Visible to Long-Wave Infrared Photodetection. ACS Applied Materials and Interfaces, 13 (32), pp.38544-38552. https://doi.org/10.1021/acsami.1c13268.

Copper Tetracyanoquinodimethane (CuTCNQ): A Metal-Organic Semiconductor for Room-temperature Visible to Long-Wave Infrared Photodetection

Sivacarendran Balendhran[1], Zakir Hussain[2], Vivek R. Shrestha[1], Jasper Cadusch[3], Ming Ye[3], Nima Sefidmooye Azar,[3] Hyungjin Kim[4,5], Rajesh Ramanathan[2], James Bullock[3], Ali Javey[4,5], Vipul Bansal[2,], and Kenneth B. Crozier[1,3,6,]**

[1]School of Physics, The University of Melbourne, Victoria 3010, Australia.

[2]Sir Ian Potter NanoBioSensing Facility, NanoBiotechnology Research Laboratory (NBRL), School of Science, RMIT University, Victoria 3001, Australia.

[3]Department of Electrical and Electronic Engineering, The University of Melbourne, Victoria 3010, Australia.

[4]Electrical Engineering and Computer Sciences, University of California at Berkeley, Berkeley, California 94720, USA.

[5]Materials Sciences Division, Lawrence Berkeley National Laboratory, Berkeley, California 94720, USA

[6]ARC Centre of Excellence for Transformative Meta-Optical Systems, University of Melbourne, Victoria 3010, Australia.

KEYWORDS: CuTCNQ, photodetectors, visible, mid infrared, metal-organic semiconductor.

ABSTRACT: Mid-wave and long-wave infrared (MWIR and LWIR) detection play vital roles in applications that include health care, remote sensing and thermal imaging. However, detectors in this spectral range often require complex fabrication processes and/or cryogenic cooling and are typically expensive, which motivates the development of simple alternatives. Here, we demonstrate broadband (0.43-10 μm) room temperature photodetection based on CuTCNQ, a metal-organic semiconductor, synthesized via a facile wet chemical reaction. The CuTCNQ crystals are simply drop cast onto interdigitated electrode chips to realize photoconductors. The photoresponse is governed by a combination of inter-band (0.43-3.35 μm) and mid-gap (3.35-10 μm) transitions. The devices show response times (~365 μs) that would be sufficient for many infrared applications (e.g. video rate imaging), with a frequency cut-off point of 1 kHz.

1. INTRODUCTION

Semiconductor photodetectors play a pivotal role in applications that include imaging, telecommunications, sensing and monitoring. These applications span wavelengths from the visible to the long-wave infrared. For photodetection in the visible range, Si is the typical material of choice due to its excellent responsivity, stability and the ease with which it can be integrated with Si electronics to produce image sensors and spectrometers.[1-3] For high performance infrared photodetection, InGaAs (near- and shortwave infrared: NIR and SWIR) and HgCdTe (mid- and long-wave infrared: MWIR and LWIR) are frequently employed.[4-5] However, these technologies often require complex fabrication processes (e.g. to achieve lattice matching and stoichiometry control) and/or cryogenic cooling.[6] Alternatives include quantum well infrared photodetectors (QWIP), type II super lattice structures (T2SLS), barrier infrared detectors (BIRD) and microbolometers. These operate over specific spectral bands defined by material and other choices, rather than being broadband.[4, 7] To date, microbolometers have been the main solution for cost-

effective room temperature MWIR and LWIR range photodetection, but they still suffer slow response times (15-20 ms).[8] Although these technologies work well for many applications, broadband (visible to LWIR) photodetectors that can be fabricated inexpensively and achieve faster response times could enable new applications, for example in very compact optical systems such as on-chip spectrometers that could be incorporated into smartphones, tablets and drones.[9]

Two-dimensional (2D) materials are promising candidates for photodetectors due to their self-terminating lattice structure. This allows the formation of thin heterostructures by simply stacking layers of 2D materials on top of one another, eliminating any requirement of lattice matching or surface passivation techniques.[10] The 2D nature of such materials can result in significant size reduction enabling field deployable compact optical devices.[9, 11] Some 2D materials show very high carrier mobilities at room temperature, making them ideal for high speed photodetection. Graphene is extensively explored due to its gapless nature, enabling photoinduced charge carrier generation over a broadband spectral range, from ultraviolet to far infrared.[12] These devices, however, suffer poor optical absorption in the MWIR/LWIR range (~2.3%) due to the single atomic layer thickness of graphene.[13-14] To increase the absorption, complex structures such as optical antennas, plasmon resonance structures or micro/nano-cavities can be used.[15-16] This increases the fabrication difficulty and the cost of such detectors, and often leads to a narrowband response. Recently, narrow bandgap semiconductors such as black phosphorus and noble metal dichalcogenides and semimetals have been used in MWIR photodetection.[17-20] Black phosphorus (bP) has been demonstrated to have photoresponse for wavelengths between 0.4-4 μm,[17, 21-24] while devices based on alloying bP with arsenic (bAsP) have shown photoresponse out to 8.2 μm.[21, 25] However, the synthesis of bulk crystals of bP and bAsP involves chemical vapor transport methods over a long period of times or high-pressure and temperature deposition processes.[21, 26] Most of

the narrow bandgap 2D materials rely on mechanical exfoliation of the bulk crystals, followed by a high yield transfer process for 2D device fabrication.[19, 21, 27-28] Furthermore, bP photo-oxidizes in ambient conditions, which is detrimental for device performance as it rapidly converts into PO_x.[29-31] This can be mitigated via additional surface passivation steps such as chemical treatment or dielectric capping,[32-33] which increases fabrication complexity. One may therefore conclude that while progress has been made, there is still much to be done to realize photodetectors that operate over a wide range of wavelengths at room temperature and can be manufactured in a simple and cost-effective manner.

Organic/metal-organic materials, however, are an attractive solution to the aforementioned challenges, as they offer low cost material synthesis, scalable device fabrication processes and integration capabilities with flexible platforms.[34-35] Copper tetracyanoquinodimethane (CuTCNQ) is a narrow bandgap metal-organic semiconductor (**Figure 1a**) with broadband optical absorption.[36-37] Its band gap is reported to be in the range of 0.137 – 0.37 eV, depending on the approach employed for bandgap estimation.[36-37] Its use for UV detection has been reported previously.[38] Although NIR photoresponse of CuTCNQ has been reported in a study of photocatalysis,[37] photodetectors have not been developed. Its synthesis is simple and scalable, being based on processes such as chemical vapor deposition or wet chemical reactions.[39-42] In this work, we investigate the viability of CuTCNQ for room temperature broadband (visible to LWIR) photodetection using a simple device architecture. We simulate the thickness dependent optical absorption of CuTCNQ to support our material of choice and the adopted device architecture for LWIR photodetection. We produce CuTCNQ photodetectors in an inter-digitated electrode (IDE) device architecture (Figure 1b) via a simple drop cast process. Our devices show photoresponse to

a broad range of wavelengths from visible (430 nm) to LWIR (10 µm). The devices show sub-millisecond rise times (of 365 µs) and a -3 dB roll-off frequency of 1 kHz at λ = 2.2 µm.

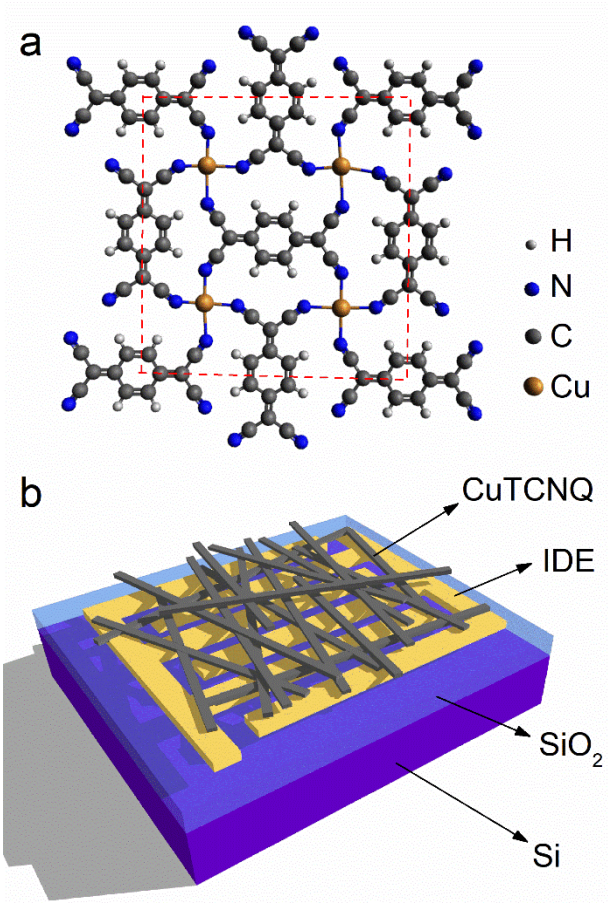

Figure 1. (a) Crystal structure of Phase 1 CuTCNQ. (b) Schematic illustration of photodetector realized in this work.

2. RESULTS AND DISCUSSION

CuTCNQ crystals are synthesized by a wet chemical reaction between copper iodide and neutral TCNQ ($TCNQ^0$) in acetonitrile (details in Experimental section).[39] The reaction process is described as follows:

$$Cu_2I_{2(aq)} + 2TCNQ_{(aq)} \longrightarrow 2CuTCNQ_{(s)} + 2I_{(aq)} \quad (1)$$

Briefly, $TCNQ^0$ has a large electron affinity of 3.38 eV that facilitates its spontaneous reduction by CuI to form $TCNQ^-$ anion, the latter reacting with Cu^+ cation to produce ionic crystals of Phase I CuTCNQ, within 3 minutes. The as-synthesized crystals are characterized to determine their structural and compositional integrity. **Figure 2a** shows a scanning electron microscopy (SEM) image of drop cast CuTCNQ crystals. Needle-shaped structures with large aspect ratios (length: width >20) are observed, suggesting the presence of Phase I CuTCNQ crystals.[37] Phase 2 crystals occur in short platelet-shaped structures (length: width of approximate unity), and are produced either during prolonged wet-chemical reactions between the same precursors or by exposure of Phase I CuTCNQ to high temperatures in acetonitrile.[39] Since Phase I exhibits a narrow bandgap, we stop the synthesis process prior to the formation of Phase II crystals. We carry out energy dispersive x-ray (EDX) spectroscopy to analyze the material composition. The EDX spectrum (Figure 2b) shows peaks corresponding to C Kα (0.28 keV), N Kα (0.39 keV) and Cu Lα (0.93 keV), which is consistent with the presence of $TCNQ^-$ and Cu^+.[39, 42] The absence of O peaks affirms the lack of any CuO_x in the material which is consistent with the high electron affinity of TCNQ,[43] resulting in higher compositional stability in the form of CuTCNQ. The material (CuTCNQ) is further characterized by comparing its measured Raman spectrum to that measured from $TCNQ^0$ precursor. Raman peaks known to be characteristic of C=CH bending and C=C ring

stretch vibrational modes of TCNQ are observed for $TCNQ^0$ and the as-synthesized crystals (of CuTCNQ) at 1202 and 1600 cm^{-1}, respectively (Figure 2c). However, the C–CN wing stretch (at 1370 cm^{-1}) and C ≡ N stretch (2202 cm^{-1}) modes are observed to be red-shifted from those measured from the $TCNQ^0$ sample (at 1450 and 2222 cm^{-1}, respectively). Based on literature,[42, 44] we attribute these red-shifts to the characteristics of CuTCNQ, which originates from the charge transfer between of Cu^+ and $TCNQ^-$. Such red-shifts and the absence of additional $TCNQ^0$ peaks at 1450 and 2222 cm^{-1} indicate the high purity of CuTCNQ employed in this study. Figure 2d presents the measured reflectance spectrum of the as-synthesized CuTCNQ. The positions of the spectral features observed in the reflectance spectrum of the as-synthesized CuTCNQ are consistent with previous reports.[45-46] In particular, the distinctive reflectance spectral feature at 12.12 µm further confirms the presence of Phase I CuTCNQ.[42]

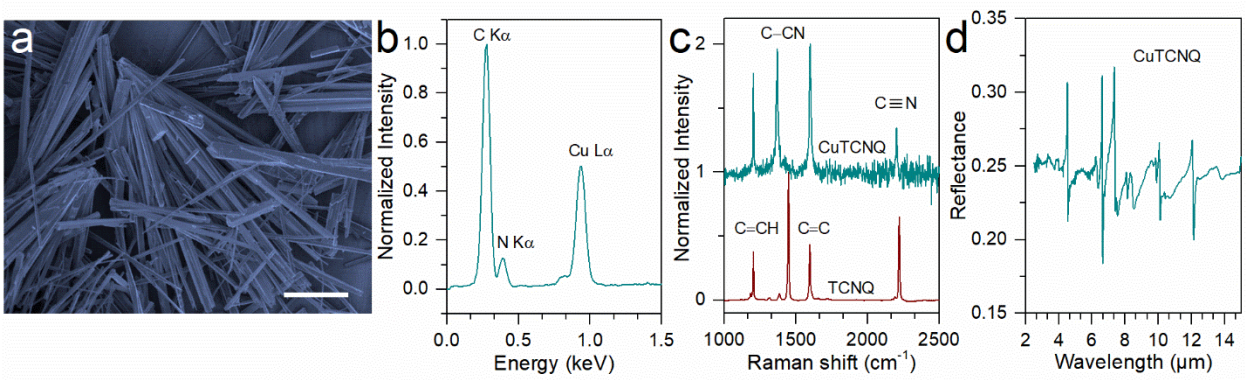

Figure 2. Material characterization: (a) SEM image of drop cast CuTCNQ crystals. Scale bar is 10 µm. (b) EDX, (c) Raman and (d) FTIR spectra of drop cast CuTCNQ crystals. EDX and Raman spectra have been normalized to their highest peak intensity values.

To predict the thickness dependent optical absorbance and reflectance in CuTCNQ, we carry out electromagnetic simulations using the finite-difference time-domain (FDTD) method. As the

dropcast process results in CuTCNQ crystals randomly oriented across all three dimensions (Figure 2a), it is difficult to model the fabricated devices. We thus consider a simplified model in which we take the CuTCNQ to be a planar film and calculate its absorption spectrum as a function of thickness. We consider three configurations (**Figure 3a**), which are as follows. Configuration 1: Freestanding CuTCNQ crystal, to quantify the intrinsic optical absorbance. Configuration 2: CuTCNQ crystal suspended on SiO_2/Si substrate, to assess the effect of the substrate excluding the IDE. Configuration 3: CuTCNQ crystal on IDE/SiO_2/Si, to mimic the experimental IDE device architecture. In each case, the thickness of CuTCNQ is varied from 0.1 to 2 μm, in steps of 100 nm. We consider this range of thicknesses as our SEM analysis shows that single crystals of CuTCNQ are within this range. As the thickness/width of the CuTCNQ crystals are larger than 100 nm, we exclude quantum confinement effects. The results, i.e. absorption in CuTCNQ for the three configurations as a function of wavelength and thickness, are shown as Figure 3b. To compare the results for these configurations, we consider the example of the CuTCNQ crystal being 1 μm thick. Refer to Supporting Information Figure S1 and Table S1 for the corresponding absorption line plots and average absorption values. For the freestanding CuTCNQ crystal (configuration 1) the absorption is seen to be above 80% in the range of 0.4 to 2 μm, with a broad peak occurring at 760 nm. In the MWIR and LWIR range, weaker absorption peaks (20-30%) are observed at 4.54, 6.4, 7.45 and 8.45 μm. In configuration 2, an enhancement in the absorbance in the MWIR and LWIR range is seen (compared to configuration 1), due to the substrate acting as an optical cavity back reflector. In configuration 3, a further enhancement in the absorption is observed in the MWIR and LWIR range, owing to the back-reflection from the Au electrodes. Since the absorption in CuTCNQ for configuration 1 is greater than 80% in the visible to SWIR range, we do not expect that the addition of a back-reflector would make a substantial difference. This is confirmed by our

modelling that predicts that the absolute increase in absorption (ΔA) is ~3% in the visible to SWIR range (0.4-2µm) for configuration 3 compared to freestanding CuTCNQ. For the MWIR range (2-5 µm), the average absolute increase in absorption ΔA is 8 %, while for the LWIR range (5-9 µm) the increase is more significant (20%). For configuration 3 (CuTCNQ on IDE), the average LWIR absorption (5-9 µm) is thus approximately twice that of freestanding CuTCNQ. This is a significant level of enhancement, confirming the potential of this device architecture for LWIR photodetection.

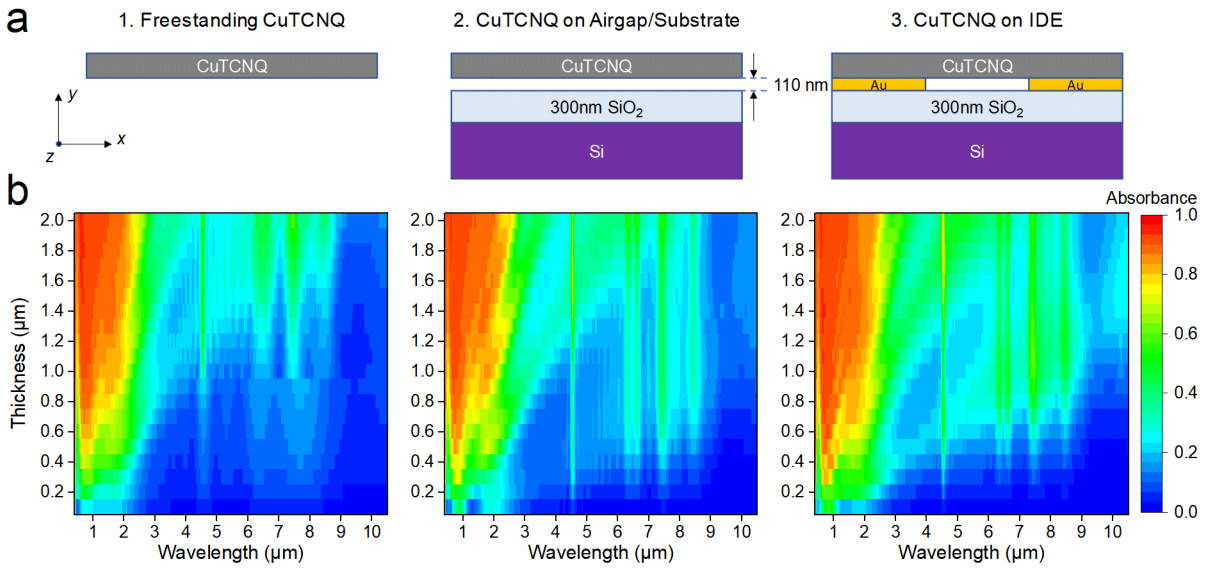

Figure 3. (a) Schematic illustration of the simulated CuTCNQ structures and (b) their absorbance spectra, plotted as a function of wavelength and thickness. Incident wave is unpolarized and is at normal incidence.

Motivated by the broadband absorption predicted by simulations, we proceed to realize photodetectors based on CuTCNQ crystals. IDE chips are fabricated via standard photolithography processes and packaged into 28-pin chip carriers. To produce a photodetector device, multiple droplets of acetonitrile (in which the CuTCNQ crystals are suspended) is pipetted onto a pair of

IDEs. The devices are dried under ambient conditions. This completes the fabrication process. Refer to the Experimental section for further details on the device fabrication process. **Figure 4a** presents optical microscope images of the device before and after the drop cast process. We bias the device using a transimpedance amplifier and characterize the photoresponse to modulated illumination using an oscilloscope and a lock-in amplifier. Refer to the Experimental section for further details. Figure 4b shows the measured photocurrent vs. time, with the illumination laser (wavelength: 2.2 μm, illumination intensity: 1.27 $mWmm^{-2}$) externally triggered using a square wave (4 V, 200 Hz). We find the rise and fall times to be 365 and 385 μs, respectively, at a bias of 2 V. We characterize the photoresponse of a commercial MCT detector under the same illumination conditions, to confirm that the measured response times of our devices are not limited by the bandwidth of the experimental setup (refer to Supporting Information Figure S2). Figure 4c presents the frequency response of the device plotted in a dB scale ($20\times\log(I/I_0)$), measured using modulated illumination (wavelength: 2.2 μm). The -3 dB roll-off point is found to be 1 kHz and is in agreement with the measured rise time ($f_{-3\,dB} \approx \frac{0.35}{t_r}$). We characterize multiple photodetectors to demonstrate the reproducibility of the devices (Supporting Information Figure S3 and Table S2). We find that the devices show rise times, fall times and cut-off frequencies that average 393 μs, 446.5 μs, and 841.8 Hz, respectively. Figure 4d shows the current-voltage (*I-V*) characteristics and the bias dependent LWIR photoresponse at λ = 8.35 μm (100 $mWmm^{-2}$). The near-linear behaviour of the measured *I-V* characteristics indicate that the CuTCNQ-Au contact is approximately ohmic and it forms a symmetric metal-semiconductor-metal junction (Supporting Information Figure S4). The photoresponse increases linearly with bias voltage. A normalized photocurrent to dark current ratio, defined as the ratio between the responsivity to dark current, is measured to be ~4 W^{-1} for 8.35 μm (100 $mWmm^{-2}$) illumination, with very little variation as the

bias is varied from 0.1 to 4 V (refer to Supporting Information Figure S5). Figure 4e shows the dependence of the LWIR photoresponse on the optical power density, at a bias of ~2 V. Photocurrent is observed to be sub-linear with a power law relationship of $I_{ph} \propto P^{0.81}$. We characterize the photoresponse and spectral responsivity of our devices using a Xenon source (430-1500 nm) and a blackbody source from a FTIR (1.5-10 μm). Refer to the Methods section for detailed experimental information. The spectral photoresponsivity is plotted in Figure 4f (left axis). The responsivity shows a steep declining trend from ~3.54 μm. This indicates an interband strong absorption edge at 3.54 μm (bandgap 0.35 eV), which is consistent with Mohammadtaheri *et al's* bandgap estimation of 0.37 eV.[37] We note that the CuTCNQ crystals do not cover the IDE in a uniform manner (Figure 4a). The coverage is incomplete and there are gaps between crystals. This is due to the stochastic nature of the dropcast process and coffee ring effect during the drying process. However, we assume the coverage is 100% and the photosensitive area to be 250×250 μm^2 for estimating the lower limit of the device responsivity and detectivity. We anticipate that methods (e.g. contact printing)[47-48] to obtain more uniform coverage would be a fruitful area for future research, as these would likely increase the responsivity and detectivity. To estimate the detectivity we experimentally characterize the noise current density (Supporting Information Figure S6). The detectivity (D^*) of the photoconductor is calculated using the following equation:[21, 49]

$$D^* = \frac{R_\lambda \sqrt{A.\Delta f}}{i_n} \qquad (2)$$

where, R_λ is the wavelength dependent responsivity, A is the device area (250×250 μm^2), Δf is the bandwidth and i_n is the noise current. We characterize D^* at a modulation frequency of 200 Hz to minimize *1/f* noise and present it in Figure 4f. The detectivity values are in the range of 10^5 to 10^6 cm $Hz^{0.5}$ W^{-1}. These are modest values. We attribute this to the low spectral responsivity,

which originates partly from incomplete CuTCNQ coverage of the IDE area. We compare the percentage coverage to the obtained photoresponse (Supporting Information Figure S7). The predominant trend is that the devices with greater coverage show greater photoresponse. We assess the stability of our devices over time, by measuring the LWIR photoresponse of 17 devices to chopped illumination at 8.35 μm (Supporting Information Figure S8). The average photoresponse normalized to day 1 shows < 3% variation over 15 days, indicating the devices remain stable over time. In addition, we characterize the ambient effects on the LWIR photoresponse (λ = 8.35 μm). We observe a notable enhancement (on average 5.75×) of the photoresponse under vacuum (Supporting Information Figure S9). We attribute this to oxygen and humidity induced channel doping, typically seen in *n*-type semiconductors. Free carriers in *n*-type semiconductors have been observed to participate in oxygen and humidity absorption, which increases the hole concentration in the channel.[50-51] This will result in increased recombination of photogenerated electrons, resulting in a reduced photoresponse. If oxygen and humidity-induced doping occur under ambient conditions, one would therefore expect the photoresponse to be enhanced when the device is in vacuum. This is consistent with our observations.

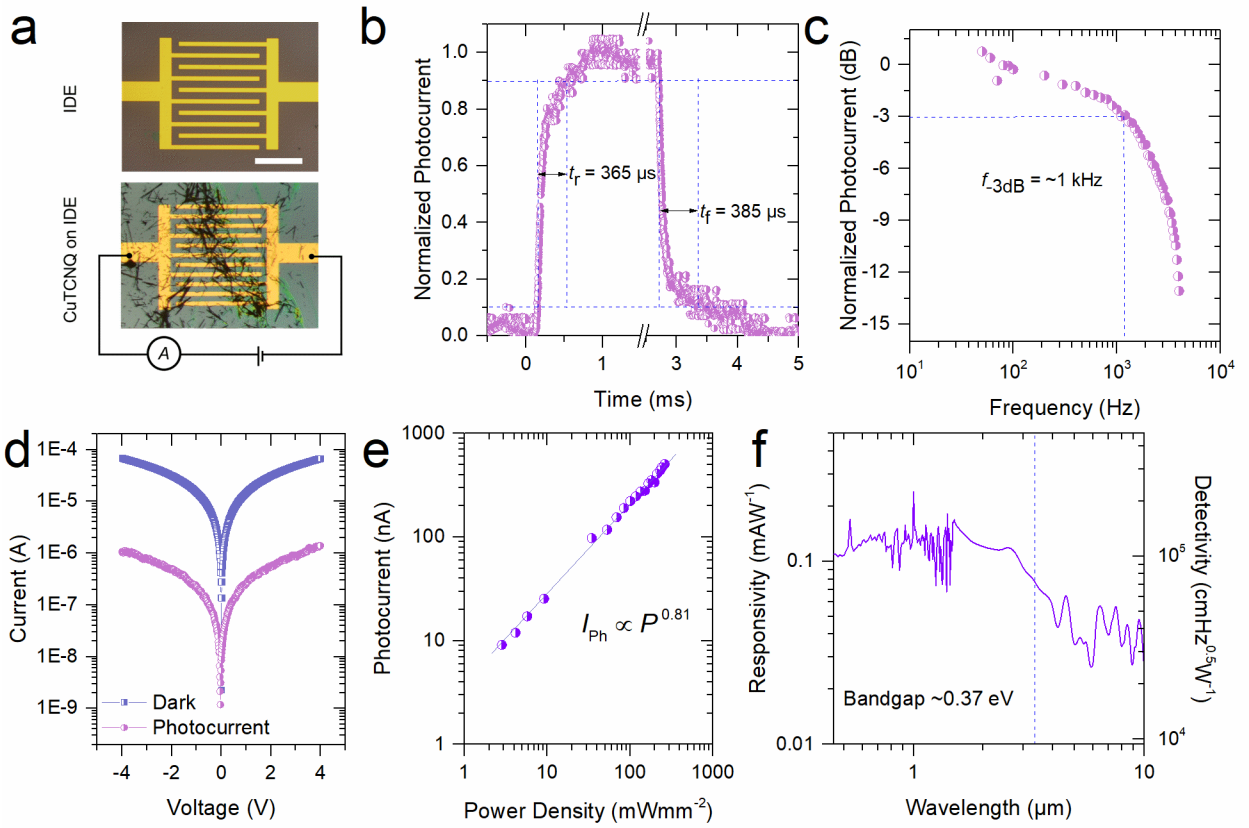

Figure 4. Photodetector characterization: (a) Optical microscope images of IDE structures before and after CuTCNQ crystals are drop cast. Scale bar is 100 µm. (b) Photocurrent vs. time and (c) frequency response for pulsed illumination at λ = 2.2 µm (1.27 mWmm^{-2}), with rise time, fall time and cut-off frequency as indicated. (d) Current-voltage characteristics and the voltage dependent photoresponse at λ = 8.35 µm (100 mWmm^{-2}). (e) Photocurrent vs. optical power density at λ = 8.35 µm. (f) Responsivity (left axis) and detectivity (right axis) vs. wavelength. Bias voltage is 2 V.

To determine the mechanism governing the photoresponse, we characterize the infrared photoluminescence (IRPL) of drop cast CuTCNQ crystals. Figure 5a compares the IRPL spectrum with a Tauc plot obtained using the extinction coefficient values used in our simulations. The Tauc plot is consistent with the bandgap estimation by Mohammadtaheri *et al*,[37] showing a strong a

strong absorption tail at ~ 0.37 eV. The lack of a strong PL peak near the band edge suggests that CuTCNQ possesses an indirect bandgap. A report from Heintz *et al*.[36] estimates the electronic bandgap of CuTCNQ to be ~0.137 eV, based on an Arrhenius plot derived from the temperature dependent electrical conductivity. This approach underestimates the bandgap in extrinsic semiconductors due to the presence of localized surface and gap states. The Tauc plot shows absorption features in the Urbach tail region suggesting that the MWIR and LWIR absorption peaks in CuTCNQ originate from such localized gap states. These absorption features strongly correlate to the peaks observed in the IRPL spectrum. This suggests that radiative recombination occurs in the MWIR-LWIR range (0.3 - 0.1 eV), facilitated by localized gap states. We plot the measured spectral responsivity with the simulated absorption and measured reflectance of a CuTCNQ on IDE device, in the MWIR and LWIR region (Figure 5b). It can be seen that the absorption and reflectance features correlate well with the measured responsivity, suggesting that the MWIR and LWIR photoresponse is due to photoexcitation of localized gap states. The sharp decline in responsivity at ~3.35 μm is indicative of the strong absorption tail at ~0.37 eV, which consistent with our bandgap estimates and literature.[37] The measured reflection dips at 4.54 and 8.49 μm also coincide with the peaks in observed in the responsivity and simulated absorption spectra, which further validates our hypothesis. Note that the absolute reflectance value cannot be compared with the simulations, as the latter only model uniform thin films of CuTCNQ rather than the complex arrangement of needle-like crystals that result from the dropcasting process. Based on these results, we ascribe the photoresponse mechanism to photoexcited electron-hole pair generation from the valence band ($\lambda \leq 3.35$ μm) and mid-gap states ($\lambda > 3.35$ μm) to the conduction band. Figure 5c schematically illustrates a simplified band diagram of a metal-semiconductor-

metal structure of our CuTCNQ on IDE device architecture and the photoresponse mechanism under bias.

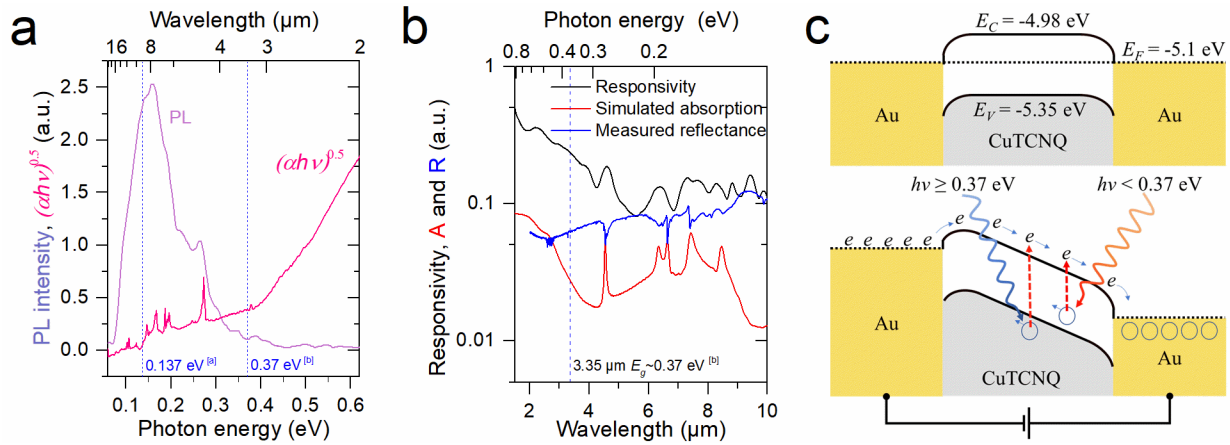

Figure 5. (a) Infrared photoluminescence spectrum and Tauc plot spectrum. The latter is extracted from the wavelength dependent extinction coefficient values. (b) Measured photoresponse spectrum, simulated absorption spectrum and measured reflectance spectrum of a CuTCNQ device. (c) Schematic of band diagram of the metal-semiconductor-metal interface of a CuTCNQ device under equilibrium (top) and with external bias (bottom). Photoresponse mechanism is illustrated for photon energies smaller and larger than the bandgap.

3. CONCLUSION

In summary, we have demonstrated a broadband metal-organic photodetector (visible-LWIR) based on drop cast CuTCNQ crystals. The material synthesis and device fabrication processes are facile, cost-effective and scalable. Our photodetectors operate at room temperature and with response times (e.g. rise time 365 μs) that are relatively fast in comparison to some other uncooled IR detectors such as VO_x based bolometers. Our simulation and experimental results show that optical absorption of CuTCNQ can be engineered to cater for photodetection over a broadband

range from ~0.43 to 10 μm. We show the applicability of CuTCNQ as an excellent candidate for room temperature, low-cost, and broadband (visible-LWIR) photodetectors. By producing photosensitive channels with uniform coverage of CuTCNQ crystals, we envision that the responsivity and detectivity can be further improved. Considering that CuTCNQ in the current work is the first example for the application for a metal-organic semiconductor as a room-temperature broadband photodetector operating in the LWIR range, the expanding library of TCNQ-based charge transfer coordination polymers throws open an exciting possibility for advancing the field of broadband IR photodetectors.

4. METHODS

Material synthesis and characterization. Phase I CuTCNQ crystals are synthesized via a wet chemical reaction between 5 mM each of copper iodide and $TCNQ^0$ in acetonitrile at 75 °C for 3 min.[39] This results in the precipitation of dark blue crystals which are washed first in acetonitrile to remove potentially unreacted $TCNQ^0$, then in de-ionized water to remove any unreacted copper and iodide ions. The crystals are then dried in vacuum at room temperature. SEM images are obtained using a FEI Verios 460L FE-SEM, at an accelerating voltage of 10 kV. EDX analyses are carried out with the SEM using an EDX Oxford X-Max Silicon Drift Detector. A Perkin–Elmer D100 spectrophotometer in attenuated total reflectance mode, with a resolution of 4 cm^{-1} is used for the FTIR spectroscopy. Raman spectroscopy is carried out with a Perkin–Elmer Raman Station 200F, at an excitation wavelength of 785 nm and with a spot size of 100 μm. Infrared photoluminescence spectrum is measured using a FTIR (iS50, Thermo Fisher) equipped with a liquid N_2-cooled HgCdTe detector. The excitation wavelength is 638 nm and the PL spectra was collected with a 15× reflecting objective.

Electromagnetic simulations. Two dimensional simulations of the absorbance and reflectance in CuTCNQ are carried out using the finite difference time domain method (FDTD) with a commercial package (Lumerical FDTD Solutions, 2019). A plane wave source (0.45-10.5 μm) at normal incidence is used. Waves polarized along x- and z-directions are considered to determine the average absorbance for an unpolarized incident wave. Periodic boundary conditions are used at the x-direction boundaries (period: 25 μm). The Au stripes of the IDE are 10 μm wide and 110 nm thick. Perfectly matched layer (PML) boundaries are used at the y-direction boundaries, which allows us to simulate the free space above the device and the bottom silicon substrate. The frequency dependent complex refractive index of CuTCNQ is from Querry (Supporting Information Figure S10),[46] while those of SiO_2 and Si and Au are obtained from Palik.[52]

Device fabrication. IDE device patterns are produced via photolithography (MLA150, Heidelberg Instruments) on 300 nm SiO_2/Si substrates coated with AZ1512 photoresist. After exposure, AZ726 developer is used to develop the electrode patterns. Chromium (10 nm thick) and gold (100 nm thick) are deposited via electron beam evaporation. The IDEs are realized after lift-off in acetone. Each fabricated IDE chip is packaged in a 28-pin dual in-line chip carrier. CuTCNQ crystals are suspended in acetonitrile (1 $mgml^{-1}$) and drop cast onto the IDE structures using a micro pipette. Approximately three 10 μl droplets are drop cast per cm^2 until acceptable level of IDE coverage is achieved. The devices are dried under ambient conditions.

Visible-SWIR photoresponse characterization. A Xenon lamp is used with a monochromator (Cornerstone 260i, Newport) to vary the illumination between 430 to 1500 nm, steps of 10 nm. A 750 nm high pass filter is used in the beam path for wavelengths ≥ 760 nm, for filtering the second order wavelengths through the monochromator. A visible-NIR objective (magnification 50×) is used to focus the light onto the device. The photodetectors are biased (2V) using a transimpedance

amplifier (TIA, SRS 570), with the dark current offset to zero. The light beam is mechanically chopped at a 110 Hz and the photocurrent is measured with a lock-in amplifier (LIA, SRS 860). The illumination power density at the focal plane is measured through a pinhole aperture (500 μm), using a power meter (Thorlabs, PMD100) equipped with calibrated Si (430-750 nm; Thorlabs, S121C) and Ge (750 -1500 nm; Thorlabs, S122C) photodiodes.

MWIR-LWIR photoresponse characterization. MWIR-LWIR photoresponse is characterized using an FTIR spectrometer (Frontier, Perkin Elmer). Illumination from the blackbody source is passed through the Michelson interferometer of the FTIR and focused onto the photodetector under test using a reflecting objective (magnification 40×). The photodetectors are biased using a TIA, with the dark current offset to zero. The amplified photoresponse is input to the external detector interface of the FTIR. The photodetector photoresponse vs wavelength (I_{CuTCNQ}) is thus obtained using the FTIR, but still needs to be calibrated for the source spectrum and power. The relative intensity of the blackbody source (I_{DTGS}) is measured using the internal deuterated triglycine sulfate (DTGS) detector of the FTIR. The photoresponsivity of the device is then calculated as I_{CuTCNQ}/I_{DTGS}. This correctly accounts for the spectrum of the source, but the power still needs to be calibrated for. This is done using a calibrated Ge photodiode (Thorlabs, FDG03) to measure the power. Refer to Supporting Information Figure S11 for a schematic illustration of the experimental setup. The noise in the raw responsivity spectrum is filtered by using a locally weighted scatterplot smoothing approach. The raw photoresponse data in the MWIR-LWIR range is compared with the measurement noise floor and presented as Supporting Information Figure S12. Noise floor measurements are carried out under the same bias conditions without the modulated IR illumination.

Device performance characterization. For further device characterization, we use MWIR and LWIR laser sources at 2.2 and 8.35 μm wavelengths, respectively. For all measurements, the photodetectors are biased (2 V) using the TIA, with the dark current offset to zero. Frequency response and time resolved photoresponse are measured using modulated illumination at a wavelength of 2.2 μm (intensity: 1.27 $mWmm^{-2}$). LWIR photoresponse as a function of power density is characterized using mechanically chopped illumination at 8.35 μm. The laser beam is focused on the photodetector under test using a reflecting objective (magnification 10×). Sixteen photocurrent measurements are performed at each laser power. These are averaged. The optical power incident on the device is controlled by varying the laser driving current. The optical power incident upon the IDE device is measured using a power meter (Thorlabs, PM100D) equipped with a broad band thermal sensor (Thorlabs, S401C). The device is replaced by the thermal sensor to measure the incident power. Knife edge measurements are carried out to determine the size of the LWIR laser beam (wavelength: 8.35 μm), which is taken as the distance between points at which the measured power is 10 and 90% of its maximum value. The diameter of the LWIR beam (wavelength 8.35 μm) is found to be 200 μm. The IDE device area is 250×250 μm^2. This is taken as the photosensitive area of the device. Note that due to the partial coverage of the IDE area by the CuTCNQ crystals, the material photoresponsivity will be underestimated. The current-voltage (*I-V*) characteristics of the devices are measured using a source measure unit (SMU, Keithley 2450). The normalized photocurrent:dark current were calculated by repeating the *I-V* measurements under dark and 8.35 μm illumination (100 $mWmm^{-2}$) conditions. Current noise density is measured using a TIA and a LIA. The same amplifier gain settings (1 μAV^{-1}) as those used for photoresponse characterization are employed. The current noise density spectrum is measured sixteen times using the LIA. These measurements are averaged. Device reproducibility

measurements are carried out by repeating the LWIR photoresponse vs power density measurements (λ = 8.35 μm) on 18 devices, over two chips. Device stability measurements are carried out by repeating these measurements over multiple days. Photoresponse is normalized to the values obtained on day 1.

ASSOCIATED CONTENT

Supporting Information. Simulated absorption of 1 um thick CuTCNQ crystal, zero bias photoresponse of a commercial MCT detector, device performance reproducibility, current-voltage characteristics, voltage dependent normalized photocurrent to dark current ratio, noise current density of a CuTCNQ photodetector, Correlation between photoresponse and % coverage, device stability over time, effect of ambient air exposure, wavelength dependent complex refractive index of CuTCNQ, schematic illustration of the experimental setup and raw photoresponse data in the MWIR-LWIR range.

AUTHOR INFORMATION

Corresponding Author

* E-mail: vipul.bansal@rmit.edu.au, kcrozier@unimelb.edu.au

ACKNOWLEDGMENT

This work was supported by DARPA (HR0011-16-1-004), and by the Australian Research Council (DP210103428, DP170103477, DP180104141, FT140100577, DE150100909). This work was performed in part at the Micro Nano Research Facility (MNRF) at RMIT University in

the Victorian Node of the Australian National Fabrication Facility (ANFF). Facilities and technical support from the RMIT Microscopy and Microanalysis Facility (RMMF), a node of Microscopy Australia, is acknowledged.

REFERENCES

(1) Huang, Z. H.; Carey, J. E.; Liu, M. G.; Guo, X. Y.; Mazur, E.; Campbell, J. C. Microstructured Silicon Photodetector. *Appl. Phys. Lett.* **2006,** *89* (3), 033506.
(2) J. J. Cadusch; J. Meng; B. Craig; Crozier, K. B. Silicon Microspectrometer Chip Based on Nanostructured Fishnet Photodetectors with Tailored Responsivities and Machine Learning. *Optica* **2019,** *6*, 1171-1177.
(3) Meng, J.; Cadusch, J. J.; Crozier, K. B. Detector-Only Spectrometer Based on Structurally Colored Silicon Nanowires and a Reconstruction Algorithm. *Nano Lett.* **2020,** *20* (1), 320-328.
(4) Rogalski, A. Recent Progress in Infrared Detector Technologies. *Infrared Phys. Tehnol.* **2011,** *54* (3), 136-154.
(5) Rogalski, A.; Antoszewski, J.; Faraone, L. Third-Generation Infrared Photodetector Arrays. *J. Appl. Phys.* **2009,** *105* (9), 44.
(6) Rogalski, A.; Martyniuk, P.; Kopytko, M. Challenges of Small-Pixel Infrared Detectors: A Review. *Rep. Prog. Phys.* **2016,** *79* (4), 046501.
(7) Ciupa, R.; Rogalski, A. Performance Limitations of Photon and Thermal Infrared Detectors. *Optoelectron. Rev.* **1997,** *1997*, 257-266.
(8) Rogalski, A. Infrared Detectors for the Future. *Acta Phys. Pol. A* **2009,** *116*, 389-406.
(9) Cadusch, J. J.; Meng, J.; Craig, B. J.; Shrestha, V.; Crozier, K. B. Visible to Long-Wave Infrared Chip-Scale Spectrometers Based on Photodetectors with Tailored Responsivities and Multispectral Filters. *Nanophoton.* **2020,** *9* (10), 3197-3208.
(10) Jariwala, D.; Marks, T. J.; Hersam, M. C. Mixed-Dimensional Van Der Waals Heterostructures. *Nat. Mater.* **2017,** *16* (2), 170-181.
(11) Buscema, M.; Island, J. O.; Groenendijk, D. J.; Blanter, S. I.; Steele, G. A.; van der Zant, H. S. J.; Castellanos-Gomez, A. Photocurrent Generation with Two-Dimensional Van Der Waals Semiconductors. *Chem. Soc. Rev.* **2015,** *44* (11), 3691-3718.
(12) Koppens, F. H. L.; Mueller, T.; Avouris, P.; Ferrari, A. C.; Vitiello, M. S.; Polini, M. Photodetectors Based on Graphene, Other Two-Dimensional Materials and Hybrid Systems. *Nat. Nanotechnol.* **2014,** *9* (10), 780-793.
(13) Wang, X.; Cheng, Z.; Xu, K.; Tsang, H. K.; Xu, J.-B. High-Responsivity Graphene/Silicon-Heterostructure Waveguide Photodetectors. *Nat. Photon.* **2013,** *7* (11), 888-891.
(14) Xia, F.; Mueller, T.; Lin, Y.-m.; Valdes-Garcia, A.; Avouris, P. Ultrafast Graphene Photodetector. *Nat. Nanotechnol.* **2009,** *4* (12), 839-843.
(15) Rogalski, A.; Kopytko, M.; Martyniuk, P. Two-Dimensional Infrared and Terahertz Detectors: Outlook and Status. *Appl. Phys. Rev.* **2019,** *6* (2), 021316.
(16) Sefidmooye Azar, N.; Shrestha, V. R.; Crozier, K. B. Bull's Eye Grating Integrated with Optical Nanoantennas for Plasmonic Enhancement of Graphene Long-Wave Infrared Photodetectors. *Appl. Phys. Lett.* **2019,** *114* (9), 091108.
(17) Bullock, J.; Amani, M.; Cho, J.; Chen, Y.-Z.; Ahn, G. H.; Adinolfi, V.; Shrestha, V. R.; Gao, Y.; Crozier, K. B.; Chueh, Y.-L.; Javey, A. Polarization-Resolved Black Phosphorus/Molybdenum Disulfide Mid-Wave Infrared Photodiodes with High Detectivity at Room Temperature. *Nat. Photon.* **2018,** *12* (10), 601-607.

(18) Yu, X.; Yu, P.; Wu, D.; Singh, B.; Zeng, Q.; Lin, H.; Zhou, W.; Lin, J.; Suenaga, K.; Liu, Z.; Wang, Q. J. Atomically thin Noble Metal Dichalcogenide: A Broadband Mid-Infrared Semiconductor. *Nat. Commun.* **2018,** *9* (1), 1545.
(19) Long, M.; Wang, Y.; Wang, P.; Zhou, X.; Xia, H.; Luo, C.; Huang, S.; Zhang, G.; Yan, H.; Fan, Z.; Wu, X.; Chen, X.; Lu, W.; Hu, W. Palladium Diselenide Long-Wavelength Infrared Photodetector with High Sensitivity and Stability. *ACS Nano* **2019,** *13* (2), 2511-2519.
(20) Liu, J.; Xia, F.; Xiao, D.; García de Abajo, F. J.; Sun, D. Semimetals for High-Performance Photodetection. *Nat. Mater.* **2020,** *19* (8), 830-837.
(21) Amani, M.; Regan, E.; Bullock, J.; Ahn, G. H.; Javey, A. Mid-Wave Infrared Photoconductors Based on Black Phosphorus-Arsenic Alloys. *ACS Nano* **2017,** *11* (11), 11724-11731.
(22) Buscema, M.; Groenendijk, D. J.; Blanter, S. I.; Steele, G. A.; van der Zant, H. S. J.; Castellanos-Gomez, A. Fast and Broadband Photoresponse of Few-Layer Black Phosphorus Field-Effect Transistors. *Nano Lett.* **2014,** *14* (6), 3347-3352.
(23) Deng, B.; Frisenda, R.; Li, C.; Chen, X.; Castellanos-Gomez, A.; Xia, F. Progress on Black Phosphorus Photonics. *Adv. Opt. Mater.* **2018,** *6* (19), 1800365.
(24) Erande, M. B.; Pawar, M. S.; Late, D. J. Humidity Sensing and Photodetection Behavior of Electrochemically Exfoliated Atomically Thin-Layered Black Phosphorus Nanosheets. *ACS Appl. Mater. Interface.* **2016,** *8* (18), 11548-11556.
(25) Long, M.; Gao, A.; Wang, P.; Xia, H.; Ott, C.; Pan, C.; Fu, Y.; Liu, E.; Chen, X.; Lu, W.; Nilges, T.; Xu, J.; Wang, X.; Hu, W.; Miao, F. Room Temperature High-Detectivity Mid-Infrared Photodetectors Based on Black Arsenic Phosphorus. *Sci. Adv.* **2017,** *3* (6), e1700589.
(26) Li, L.; Yu, Y.; Ye, G. J.; Ge, Q.; Ou, X.; Wu, H.; Feng, D.; Chen, X. H.; Zhang, Y. Black Phosphorus Field-Effect Transistors. *Nat. Nanotechnol.* **2014,** *9* (5), 372-377.
(27) Suryawanshi, S. R.; More, M. A.; Late, D. J. Laser Exfoliation of 2d Black Phosphorus Nanosheets and Their Application as a Field Emitter. *RSC Adv.* **2016,** *6* (113), 112103-112108.
(28) Wang, Y.; Wu, P.; Wang, Z.; Luo, M.; Zhong, F.; Ge, X.; Zhang, K.; Peng, M.; Ye, Y.; Li, Q.; Ge, H.; Ye, J.; He, T.; Chen, Y.; Xu, T.; Yu, C.; Wang, Y.; Hu, Z.; Zhou, X.; Shan, C.; Long, M.; Wang, P.; Zhou, P.; Hu, W. Air-Stable Low-Symmetry Narrow-Bandgap 2d Sulfide Niobium for Polarization Photodetection. *Adv. Mater.* **2020,** *32* (45), 2005037.
(29) Ahmed, T.; Balendhran, S.; Karim, M. N.; Mayes, E. L. H.; Field, M. R.; Ramanathan, R.; Singh, M.; Bansal, V.; Sriram, S.; Bhaskaran, M.; Walia, S. Degradation of Black Phosphorus Is Contingent on Uv–Blue Light Exposure. *npj 2D Mater. Appl.* **2017,** *1* (1), 18.
(30) Island, J. O.; Steele, G. A.; Zant, H. S. J. v. d.; Castellanos-Gomez, A. Environmental Instability of Few-Layer Black Phosphorus. *2D Mater.* **2015,** *2* (1), 011002.
(31) Abate, Y.; Akinwande, D.; Gamage, S.; Wang, H.; Snure, M.; Poudel, N.; Cronin, S. B. Recent Progress on Stability and Passivation of Black Phosphorus. *Adv. Mater.* **2018,** *30* (29), 1704749.
(32) Kim, J.-S.; Liu, Y.; Zhu, W.; Kim, S.; Wu, D.; Tao, L.; Dodabalapur, A.; Lai, K.; Akinwande, D. Toward Air-Stable Multilayer Phosphorene Thin-Films and Transistors. *Sci. Rep.* **2015,** *5* (1), 8989.
(33) Walia, S.; Balendhran, S.; Ahmed, T.; Singh, M.; El-Badawi, C.; Brennan, M. D.; Weerathunge, P.; Karim, M. N.; Rahman, F.; Rassell, A.; Duckworth, J.; Ramanathan, R.; Collis, G. E.; Lobo, C. J.; Toth, M.; Kotsakidis, J. C.; Weber, B.; Fuhrer, M.; Dominguez-Vera, J. M.; Spencer, M. J. S.; Aharonovich, I.; Sriram, S.; Bhaskaran, M.; Bansal, V. Ambient Protection of

Few-Layer Black Phosphorus Via Sequestration of Reactive Oxygen Species. *Adv. Mater.* **2017,** *29* (27), 1700152.
(34) Li, Q.; Guo, Y.; Liu, Y. Exploration of near-Infrared Organic Photodetectors. *Chem. Mater.* **2019,** *31* (17), 6359-6379.
(35) Simone, G.; Dyson, M. J.; Meskers, S. C. J.; Janssen, R. A. J.; Gelinck, G. H. Organic Photodetectors and Their Application in Large Area and Flexible Image Sensors: The Role of Dark Current. *Adv. Funct. Mater.* **2020,** *30* (20), 1904205.
(36) Heintz, R. A.; Zhao, H.; Ouyang, X.; Grandinetti, G.; Cowen, J.; Dunbar, K. R. New Insight into the Nature of Cu(Tcnq): Solution Routes to Two Distinct Polymorphs and Their Relationship to Crystalline Films That Display Bistable Switching Behavior. *Inorg. Chem.* **1999,** *38* (1), 144-156.
(37) Mohammadtaheri, M.; Ramanathan, R.; Walia, S.; Ahmed, T.; Weerathunge, P.; Anderson, S. R.; Field, M. R.; Dekiwadia, C. D.; O'Mullane, A. P.; Gaspera, E. D.; Bhaskaran, M.; Sriram, S.; Bansal, V. Broadband Light Active Mtcnq-Based Metal–Organic Semiconducting Hybrids for Enhanced Redox Catalysis. *Appl. Mater. Today* **2018,** *13*, 107-115.
(38) Basori, R.; Raychaudhuri, A. K. Role of Contact and Contact Modification on Photo-Response in a Charge Transfer Complex Single Nanowire Device. *Nano-Mocro Lett.* **2014,** *6* (1), 63-69.
(39) Hussain, Z.; Ojha, R.; Martin, L. L.; Bond, A. M.; Ramanathan, R.; Bansal, V. Controlling the Morphological and Redox Properties of the Cutcnq Catalyst through Solvent Engineering. *Emergent Mater.* **2019,** *2* (1), 35-44.
(40) Neufeld, A. K.; O'Mullane, A. P.; Bond, A. M. Control of Localized Nanorod Formation and Patterns of Semiconducting Cutcnq Phase I Crystals by Scanning Electrochemical Microscopy. *Journal of the American Chemical Society* **2005,** *127* (40), 13846-13853.
(41) O'Mullane, A. P.; Fay, N.; Nafady, A.; Bond, A. M. Preparation of Metal−Tcnq Charge-Transfer Complexes on Conducting and Insulating Surfaces by Photocrystallization. *Journal of the American Chemical Society* **2007,** *129* (7), 2066-2073.
(42) Ramanathan, R.; Pearson, A.; Walia, S.; Kandjani, A. E.; Mohammadtaheri, M.; Bhaskaran, M.; Sriram, S.; Bhargava, S. K.; Bansal, V. Solution-Processable Do-It-Yourself Switching Devices (Diy Devices) Based on Cutcnq Metal-Organic Semiconductors. *Appl. Mater. Today* **2018,** *10*, 12-17.
(43) Usov, P. M.; Jiang, H.; Chevreau, H.; Peterson, V. K.; Leong, C. F.; D'Alessandro, D. M. Guest–Host Complexes of Tcnq and Tcne with Cu3(1,3,5-Benzenetricarboxylate)2. *J. Phys. Chem. C* **2017,** *121* (47), 26330-26339.
(44) Gucciardi, P. G.; Trusso, S.; Vasi, C.; Patanè, S.; Allegrini, M. Nano-Raman Imaging of Cu–Tcnq Clusters in Tcnq Thin Films by Scanning near-Field Optical Microscopy. *Phys. Chem. Chem. Phys.* **2002,** *4* (12), 2747-2753.
(45) Pearson, A.; O'Mullane, A. P.; Bhargava, S. K.; Bansal, V. Synthesis of Cutcnq/Au Microrods by Galvanic Replacement of Semiconducting Phase I Cutcnq with Kaubr4 in Aqueous Medium. *Inorg. Chem.* **2012,** *51* (16), 8791-8801.
(46) Querry, M. R. *Optical Constants*; CRDC-CR-85034; Defense Technical Information Center: June 1985; pp 372-384.
(47) Javey, A.; Nam; Friedman, R. S.; Yan, H.; Lieber, C. M. Layer-by-Layer Assembly of Nanowires for Three-Dimensional, Multifunctional Electronics. *Nano Lett.* **2007,** *7* (3), 773-777.

(48) Lau, P. H.; Takei, K.; Wang, C.; Ju, Y.; Kim, J.; Yu, Z.; Takahashi, T.; Cho, G.; Javey, A. Fully Printed, High Performance Carbon Nanotube Thin-Film Transistors on Flexible Substrates. *Nano Lett.* **2013,** *13* (8), 3864-3869.
(49) Vincent, J. D. *Fundamentals of Infrared Detector Operation and Testing*, Wiley-VCH: 1990; p 504.
(50) Cho, K.; Park, W.; Park, J.; Jeong, H.; Jang, J.; Kim, T.-Y.; Hong, W.-K.; Hong, S.; Lee, T. Electric Stress-Induced Threshold Voltage Instability of Multilayer Mos2 Field Effect Transistors. *ACS Nano* **2013,** *7* (9), 7751-7758.
(51) Han, P.; Adler, E. R.; Liu, Y.; St Marie, L.; El Fatimy, A.; Melis, S.; Van Keuren, E.; Barbara, P. Ambient Effects on Photogating in Mos2 Photodetectors. *Nanotechnol.* **2019,** *30* (28), 284004.
(52) Palik, E. D. *Handbook of Optical Constants of Solids*, Elsevier Acedemic Press: 1998; Vol. 3, p 653-682.

For Table of Contents Only